Research Square

Preprints are preliminary reports that have not undergone peer review.
They should not be considered conclusive, used to inform clinical practice,
or referenced by the media as validated information.

Degradation of Petroleum Hydrocarbons in Wastewater by MnFe2O4@BC Catalysts Activated with Persulfate: Investigation into Radical and Non-radical Transformation Pathways and Mechanisms

Yu He
Chongqing University of Technology
Hengyu Chen
Southwest University
Mingyang Tan
Chongqing University of Technology
Lujie He
Hangzhou Environmental Protection Science Research and Design Co. Ltd
Zhilong Diao
Chongqing Hui Ya Environmental Protection Engineering Co. Ltd
Shuang Wu
Chongqing Hui Ya Environmental Protection Engineering Co. Ltd
Shijing Liu
Chongqing Hui Ya Environmental Protection Engineering Co. Ltd
Huanfang Gao
ghf1973@cqut.edu.cn

Chongqing University of Technology

Research Article

Keywords: Persulfate, Iron- and manganese-based catalysts, Biochar, Degradation mechanism

Posted Date: September 15th, 2026

DOI: https://doi.org/10.21203/rs.3.rs-10902371/v1

License: This work is licensed under a Creative Commons Attribution 4.0 International License.
Read Full License

Additional Declarations: No competing interests reported.

Degradation of Petroleum Hydrocarbons in Wastewater by $MnFe_2O_4$@BC Catalysts Activated with Persulfate: Investigation into Radical and Non-radical Transformation Pathways and Mechanisms

Yu He [a,1], Hengyu Chen [d,1], Mingyang Tan [a], Lujie He [c], Zhilong Diao [b], Shuang Wu [b], Shijing Liu [b], Huanfang Gao [a,*]

[a] *School of Chemistry and Chemical Engineering, Chongqing University of Technology, Chongqing 400054, China*

[b] *Chongqing Hui Ya Environmental Protection Engineering Co. Ltd., Chongqing 400041, China*

[c] *Hangzhou Environmental Protection Science Research and Design Co. Ltd., Hangzhou, 310000, China*

[d] *Key Laboratory of the Three Gorges Reservoir Region's Eco-Environment (Ministry of Education), College of Resources and Environment, Southwest University, Chongqing, 400715, PR China*

[*] **Corresponding author**

E-mail address: ghf1973@cqut.edu.cn (H. Gao)

Telephone：13508352906

[1] **These authors contributed equally to this work**

Abstract: The pollution hazards of petroleum hydrocarbon wastewater are serious, and it is urgent to develop new technologies for efficient and environmentally friendly remediation and treatment. In this paper, a new composite material of ferromanganese spinel-supported biochar was prepared by the sol-gel method, and a heterogeneously activated persulfate system was constructed to degrade petroleum hydrocarbons (TPH) in water. The results showed that when the molar ratio of Fe to Mn was 4:1. The dosage of biochar was 5 g, the $MnFe_2O_4$@ wheat straw (MFBX) and $MnFe_2O_4$@ maize cobs (MFBY) catalysts had the best activation effect on sodium persulfate (PS) concentration of 15 mmol, where the degradation rates of total petroleum hydrocarbons in 24 h reaching as high as 84.44% and 88.05%. The valence cycle of Fe-Mn bimetals and biochar formed a synergistic activation effect, and the free radical pathway was dominated by $SO4^{\bullet-}$, •OH, and $O_2^{\bullet-}$, and the non-radical pathway was dominated by $^1O_2$, synergistically driving the degradation of pollutants. It provides new materials and theoretical and technical support for the efficient green remediation of petroleum hydrocarbon-polluted wastewater.

Keywords: Persulfate; Iron- and manganese-based catalysts; Biochar; Degradation mechanism

1 Introduction

In recent years, with rapid economic development, the transformation of industrialization, and urban development, many contaminated sites have been left behind, including chemical, coking, pharmaceutical, and so on[1]. In particular, as living standards have improved in recent years, the energy demand has grown significantly. During the extraction, transportation, and processing of petroleum, "spills, leaks, drips, and seepages" sometimes occur. Sudden accidents occur from time to time, causing large amounts of petroleum to enter soil and groundwater, posing a potential threat to human health and the environment[2]. Total petroleum hydrocarbons (TPH) are a mixture of various hydrocarbons, including alkanes, aromatics, and polycyclic hydrocarbons. TPH are relatively low in volatility, highly water-soluble, and poorly biodegradable; they are difficult to remove from water bodies through natural purification processes in the short term, and will inevitably cause long-term impacts[3].

Groundwater contaminated by petroleum hydrocarbons is currently treated using in-situ oxidation methods. In-situ chemical oxidation (ISCO) generally involves injecting strong oxidants into wells located upstream of the contaminated site. The oxidant migrates and disperses under the influence of the groundwater flow field and reacts with the pollutants, transforming them into non-toxic or less toxic substances, thereby achieving remediation. Activated persulfate is commonly used as a powerful oxidant, and there are various methods to activate persulfate, such as thermal activation, alkaline activation, transition metal activation, and UV activation, each with its own advantages and disadvantages[4-6]. The features of various persulfate activation approaches were presented in Table S1.

Peroxosulphates (PS) include peroxomonosulphates (PMS) and peroxodisulphates (PDS); both have a similar basic structure and contain an -O-O- bond. The intrinsic redox potentials of PMS and PDS are low, at just 1.82 and 2.01 V. Under normal conditions, it reacts very little with pollutants; external conditions are required to activate it, causing the -O-O- bond in the persulphate to break and generate the sulphate radical ($\bullet SO_4^-$), which possesses stronger oxidizing properties, thereby enabling the

degradation of pollutants[7].

Transition metals (Co, Cu, Fe, Mn, etc.) can activate persulphates to produce $\bullet SO_4^-$ through electron transfer, Among these, iron-based systems feature Fe^{2+}, which is readily oxidized to Fe^{3+} with high selectivity, low toxicity and low reaction costs; manganese-based systems exhibit excellent oxygen transfer efficiency, good environmental compatibility and multiple valence states, whilst demonstrating risk stability across various aquatic environments; furthermore, they hold broad application prospects in the field of persulphate activation[8-9]. Wang H et al. conducted experiments on the degradation of 2,4-dichlorophenol (2,4-DCP) by Fe_3O_4 prepared in the presence of activated persulphate (PMS), under visible light; 2 g/L Fe_3O_4 and 0.5 mM PMS achieved 100% degradation of 2,4-DCP within 70 min[10]. However, Fe-based catalysts have certain limitations during the degradation process: the low-valent metal ions tend to react with PS to form high-valent ions, but the conversion efficiency of the generated high-valent metal ions back to low-valent ions is low, leading to catalyst deactivation and low catalytic efficiency. Mn-based catalysts face problems such as difficult recovery, limiting their applications[11-12]. Shu min Yang et al. the activation of persulphate by iron-manganese binary oxides enables the efficient degradation of bisphenol A; when the persulphate concentration is 1.0 mM and the molar ratio of iron to manganese is 1:1, a reaction time of 60 min results in a degradation rate of 91.3% for TBBPA, Previous studies have shown that, compared to single-metal oxide systems[13], synergistic interactions between bimetallic catalysts can facilitate electron transfer, for example Fe/Co[13-14], Co/Cu[15-16], Fe/Cu[17-18] and Fe/Mn[19-20] et al, consequently, methods to enhance the activation efficiency of persulphates have gained favor among researchers.

As subsequent research has revealed, single-metal catalysts are prone to a range of issues, including oxidation, metal leaching, and agglomeration. Biochar (BC) is produced by the pyrolysis of waste biomass under anaerobic conditions. It offers advantages such as a wealth of functional groups, an excellent porous structure and a wide range of sources, and has replaced expensive carbon-based materials in

environmental remediation, by loading a bimetallic compound onto its surface, agglomeration is minimized; furthermore, by utilizing biochar inherent strong adsorption capacity and large specific surface area, as well as the presence of persistent free radicals and abundant oxygen-containing functional groups on its surface, PS can be effectively activated to generate highly reactive free radicals[21]. Hu F et al. conducted experiments to investigate the removal of organic pollutants using nitrogen-doped starch-derived porous carbon loaded with iron and manganese to deactivate PMS[22]. It was found that the rich layered structure and nitrogen doping facilitated the adsorption of BPA and PMS, with Fe and Mn acting as electron donors within the carbon layers in the forms of Fe_xC and Mn_xO_y, respectively[22]. However, there has been little research into iron- and manganese-loaded biochar for the treatment of oily wastewater.

Zhao L et al. investigated the synthesized copper-cobalt oxides for PMS activation, where the active species participate in oxidation reactions via single-electron transfer pathways with radicals and singlet oxygen as the active species, while the oxygen atom transfer pathway also plays a role[23]. Because Cu^{2+} has a strong complexing ability, it combines with PMS to form $\equiv Cu\text{-}OOSO_3^-$. The electron transfer of the Cu-O-Co bridge promotes the interaction between $\equiv Cu\text{-}OOSO_3^-$ and pollutants. This conclusion provides data support for the study of active species in pollutant oxidation[24-26]. Based on the above findings, this study employed the sol-gel method to immobilize a carbon-supported bimetallic compound ($MnFe_2O_4$) onto biochar, and used it to activate the degradation of total petroleum hydrocarbons (TPH)—a typical component of petroleum wastewater—in water. the main objectives of this study were:(1) preparation and Characterization of the $MnFe_2O_4$@BC Composite Catalyst,(2) to evaluate the catalytic performance of the $MnFe_2O_4$@BC catalyst in the degradation of total petroleum hydrocarbons (TPH) within the $MnFe_2O_4$@BC/PS system, and to optimize the degradation system by investigating factors such as catalyst loading, PS loading and the Fe: Mn molar ratio,(3) the activation and synergy mechanisms of Fe, Mn and BC in composite catalysts are described,(4)the study investigated the stability and

reproducibility of composite materials, providing a theoretical basis for their subsequent practical application.

2 Materials and Methods

2.1 Reagents and medicines

Comprehensive details regarding the materials are provided in the Supporting Information (SI) Text S1. We used the analytically pure chemical reagents purchased directly, without further purification, and all experiments were conducted using deionized water.

2.2 Material Preparation

2.2.1 Preparation of BC

The wheat straw and corn cob were air-dried under natural conditions for 72 h, and then dried in a forced-air oven at 60 °C for 24 h. Subsequently, they were ground using a grinder, sieved through a 100-mesh screen, and pyrolyzed in a muffle furnace at 400 °C in an oxygen-limited atmosphere for 4 h. The resulting products were washed 2–3 times with deionized water and finally dried at 60 °C for 8 h to obtain wheat straw biochar (BCX) and corn cob biochar (BCY).

2.2.2 Preparation of $MnFe_2O_4$@BC Composites (MFB-Biomass) via the Sol-Gel Method

The citric acid sol-gel method was employed to prepare $MnFe_2O_4$@BC composites. $Fe(NO_3)_3·9H_2O$ and $Mn(NO_3)_2·4H_2O$ with different molar ratios (e.g., a 4:1 ratio of Fe $(NO_3)_3·9H_2O$ to $Mn(NO_3)_2·4H_2O$, with mass additions of 4.04 g and 0.63 g, respectively) [2] were dissolved in a certain volume of deionized water at room temperature. Citric acid ($C_6H_8O_7$) was then added to 80 mL of deionized water at a concentration equal to the sum of the molar ratios of Fe $(NO_3)_3·9H_2O$ and Mn $(NO_3)_2·4H_2O$, and the mixture was stirred for 1 h. The pH of the solution was then adjusted to approximately 7 using $NH_3·H_2O$[27]. Meanwhile, different masses of BC were ultrasonically dispersed in deionized water for 30 min and then added to the above

solution. The mixture was stirred and heated at 100 °C to form a viscous gel, which was transferred to a muffle furnace and calcined at 400 °C for 4 h to remove citric acid[27]. The sample was washed 2–3 times with deionized water, and finally dried at 65 °C for 10 h. $MnFe_2O_4$@BC was obtained after grinding to 100 mesh. For the sake of comparison, a pure $MnFe_2O_4$ (MFB) sample was prepared under the same conditions without the addition of BC. The preparation flowchart is shown in Fig 1, and for specific preparation parameters, please refer to Table S2.

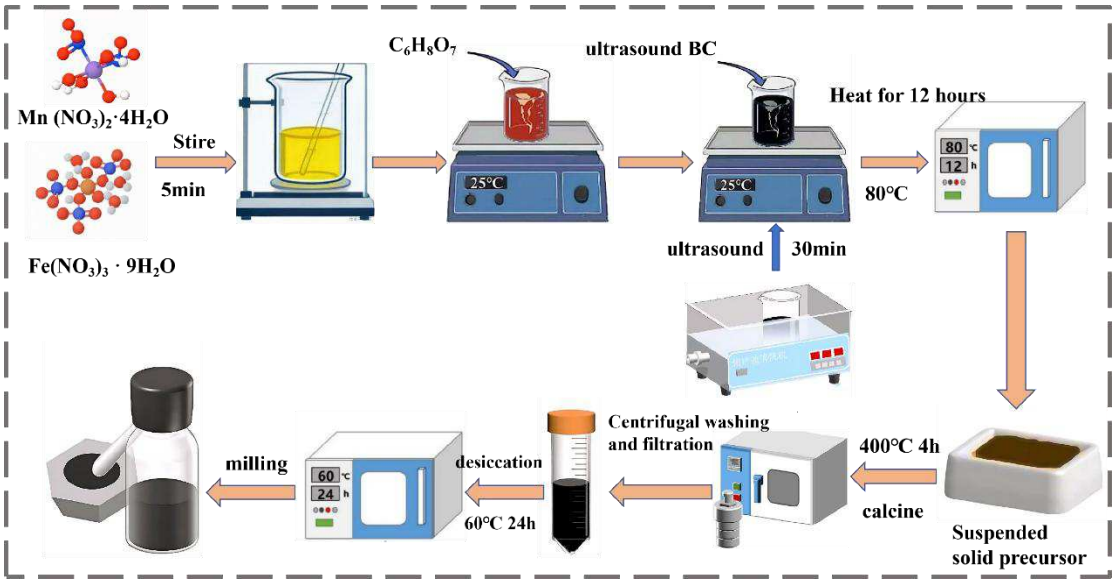


Fig. 1 Schematic diagram of the sol-gel method for the preparation of MFBY and MFBX

2.3 Material characterization

Comprehensive details regarding the materials characterization method are provided in the Supporting Information (SI) Text S2.

2.4 Degradation performance of MFBX and MFBY in wastewater

The experiment was conducted at room temperature (25 °C). In a 100 mL conical flask, 0.5 g of the reaction catalyst (MFBX/Y), 1000 mg/L of TPH, and 15 mmol/L of sodium persulfate (PS) were added. The mixture was reacted for 24 h in a constant-temperature shaking incubator at a speed of 110 rpm. Subsequently, after extraction with petroleum ether, the TPH concentration was determined using a UV spectrophotometer at a wavelength of 225 nm. The effects of key reaction parameters—including catalyst dosage, BC dosage, PS concentration, reaction time, and the iron-to-manganese metal loading ratio—on the TPH degradation rate were investigated. In this

degradation reaction, the method of controlled variables was employed, whereby one parameter was varied whilst the others remained constant. Each experimental group comprised three replicates. Experiments concerning quenching, ionic interference and catalyst stability were conducted under optimal experimental conditions, following the procedures outlined in the preceding degradation experiments.

2.5 Analytical methods

Using a UV spectrophotometer, the absorbance of the substance was measured at a wavelength of 225 nm. The calculation was performed according to Eq. (1) and Eq. (2).

$$x=\frac{A-0.0024}{0.0083} \quad \text{Eq (1)}$$

$$B=x*25 \quad \text{Eq (2)}$$

Where x (mg/L) is the post-release TPH concentration and B (mg/L) is the concentration of undiluted TPH. A (nm) is the absorption wavelength, and 25 is the dilution factor.

Calculate the leaching concentrations of iron and manganese in the material using Eq.(3).

$$C=(C_1-C_0)\times N\times 10^{-3} \quad \text{Eq (3)}$$

Where C (mg/L) is the mass concentration of iron and manganese in the material, and C_1 (mg/L) is the mass concentration of iron and manganese on the calibration curve. C_0 (mg/L) is the mass concentration of iron and manganese in the blank sample, and N is the dilution factor.

The stabilization rate for the leaching of metal ions is calculated using Eq. (4).

$$K=(1-\frac{C_1}{C})\times 100\% \quad \text{Eq (4)}$$

Where K (%) is the stabilization rate and C_1 (mg/L) is the mass concentration of iron and manganese leached from wastewater contaminated with TPH following the addition of MFBX and MFBY. C (mg/L) is the mass concentration of iron and manganese leached from MFBX and MFBY that have not reacted with the TPH wastewater.

3.1 Material characterization

To characterize the phase composition and crystallinity of the composites, the X-ray diffraction patterns of BCX, MFB, MFBX, BCY, MFBY, etc., the results were shown in Fig. 2 (a) and (b). As can be seen from Fig. 2a, the X-ray diffraction pattern of BCX exhibits broad diffraction peaks at 20.96–26.69°, which are consistent with the amorphous graphitic phase of pyrolytic BCX[28]. The diffraction peaks of MFB are at 26.7, 30.3, 35.7, 43.4, 57.3, and 62.7°, which can be attributed to the (111)、 (220)、 (311)、 (400)、 (511), and (440) crystal planes of the spinel-type MFB[29-30], indicating the preparation of high-purity, high-quality spinel-type MFB crystals[23]. As observed in Fig 2b, the X-ray diffraction patterns of MFBY and MFB are similar; however, compared to MFB, the intensity of the diffraction peaks in MFBY is significantly reduced, and there is no obvious change in the positions of the diffraction peaks between MFBY and MFB. As observed in Fig 2a, the control MFBX exhibits an X-ray diffraction pattern similar to that of MFB; however, compared to the peak intensity of MFB, the peak intensity of MFBX is considerably weaker. Furthermore, the positions of the diffraction peaks in the MFBX composite are almost identical to those of MFB, with a spinel-type (622) magnetic iron-manganese oxide crystal plane at 75.9°. A possible reason for this is that during the preparation of the MFBX and MFBY composites, the surface of the MFB particles formed an amorphous structure with BCX and BCY, thereby further demonstrating that iron and manganese in MFBX and MFBY have been successfully loaded onto BCX and BCY. The broad peaks, narrow peaks, and high-intensity peaks in the X-ray diffraction spectrum all demonstrate that the prepared MFBX and MFBY composites possess a high spinel phase content and small particle size.

As can be seen from Fig. 2 (c) and (d), the composite material (MFBY) prepared using maize cobs (BCY) as biomass to produce iron-manganese-loaded biochar, exhibits a Fe–O stretching vibration peak at 503.42 cm^{-1} relative to the original biochar, and a Mn–O stretching vibration peak at 725.23 cm^{-1}corresponding to the tetrahedral or octahedral structure of spinel $MnFe_2O_4$[29][31], The composite material (MFBX) prepared using wheat straw (BCX) as the biomass to produce iron-manganese-loaded biochar exhibits an Fe-O stretching vibration peak at 528.43 cm^{-1} relative to the original

biochar, and a Mn-O stretching vibration peak at 729.51 cm^{-1} corresponding to the tetrahedral or octahedral structure of spinel $MnFe_2O_4$, Furthermore, the MFBX and MFBY composites exhibit an absorption peak around 3400 cm^{-1}, which is attributed to the successful attachment of MFB nanoparticles to the biochar surface; which is attributed to the successful attachment of MFB nanoparticles to the biochar surface; consistent with the previous XRD results, as biochar possesses -OH functional groups, the OH^- ions in this region form a strong absorption band[28-29][31]. The vibrational peak at 1665.25 cm^{-1} is associated with the C=O stretching vibration; near 853.00 cm^{-1} there is a C-H stretching vibration; and near 1100 cm^{-1} there is a C-O stretching vibration. This is likely due to the formation of metal-O-C bonds on the surface of the MFBX and MFBY composites, thereby providing additional active sites for subsequent catalytic performance to promote the degradation of their TPH[29][32].

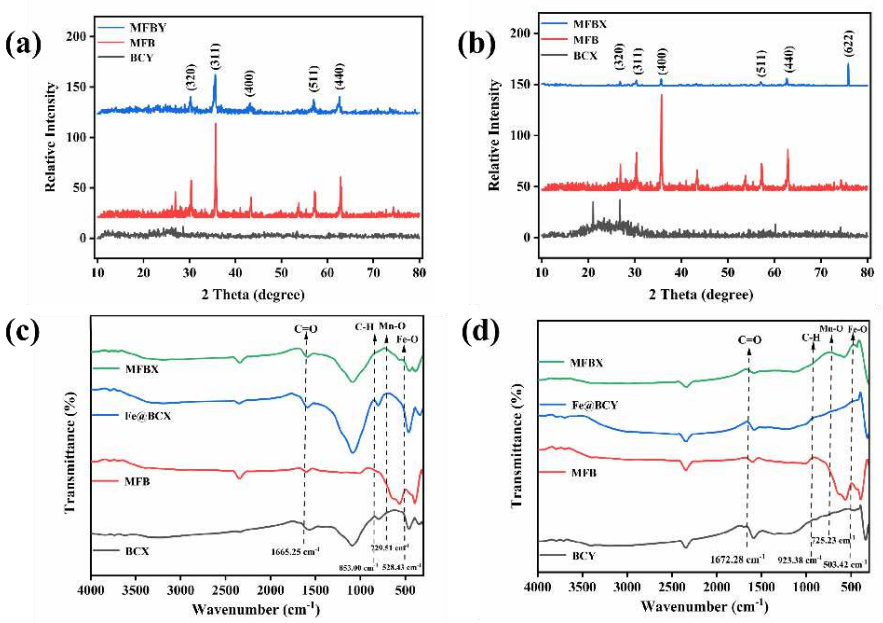


Fig. 2 XRD (a) and (b) and FT-IR (c) and (d) test results for MFBX and MFBY

The SEM images of BCX, MFB, $MFBX_{4:1}$-5, BCY, and $MFBY_{4:1}$-5 the results were shown in Fig. 3 (a–k), energy dispersive spectroscopy (EDS) of BCX, MFB, $MFBX_{4:1}$-5, and $MFBY_{4:1}$-5 are shown in Fig. 3 (l–o). Fig. 3a shows that the surface of BCX is smooth and possesses a relatively uniform microporous structure, whilst Fig. 3 (b-c)) reveal that MFB exhibits severe agglomeration, forming micro-spherical particles.

From Fig. 4a, it can be seen that the specific surface area of MFB is 50.43 m^2 /g, which is considerably lower than that of BCX (149.010 m^2 /g), resulting in fewer active sites and reduced catalytic activity. Consequently, when using biochar as a support and comparing BCX with MFBX, it was found that the morphologies of the two were markedly different: the surface of MFBX became rough, and the macropores originally present in BCX were blocked. This demonstrates that MFB has been successfully loaded onto BCX biochar; this structure is expected to facilitate the degradation of TPH by $MnFe_2O_4$@BC/PS. Fig. 3 (g–h) shows that the BCY surface is relatively rough, exhibiting a honeycomb-like porous structure. Comparing BCY with MFBY, it was observed that the overall surface of MFBY is particularly rough, and MFB micro-spherical particles have penetrated the internal pores. It can be seen that the microspheres are uniformly anchored to the surface and pore structure of BCY[27], and that the specific surface area of BCY (52.262 m^2 /g) differs only slightly from that of MFB (50.430 m^2 /g), but differs significantly from that of MFBY (152.453 m^2 /g) in Fig. 4b. Consequently, the significantly reduced aggregation of MFB in MFBY will further promote the degradation of TPH by MFBY/PS. Furthermore, energy dispersive spectroscopy (EDS) scans indicate that the surfaces of MFBX and MFBY are distributed with C, O, Fe, Mn, and Si elements in Fig. 3(I-k), and the Fe: Mn ratio (24.44:6.30) in Tables S3 and S4 is close to the designed experimental atomic ratio (4:1) in Fig. 3 (l–o).

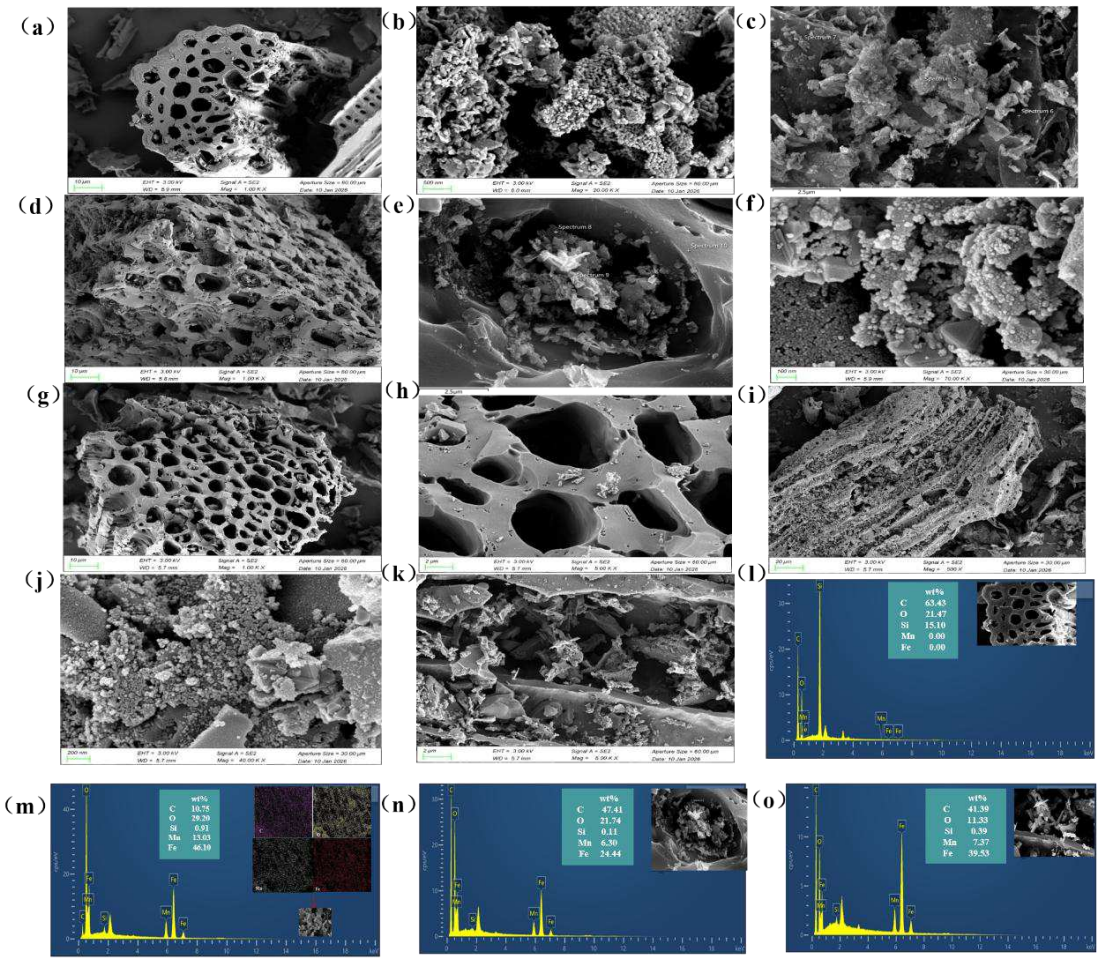


Fig. 3 SEM of BCX (a), MFB (b, c), MFBX (d, e, f), BCY (g, h) and MFBY (i, j, k), and EDS of BCX (l), MFB (m), MFBX (n) and MFBY (o)

The N_2 adsorption–desorption isotherms and corresponding pore sizes for BCX, Fe@BCX, MFB and MFBX, and for BCY, Fe@BCY, MFB and MFBY, are shown in Fig. 4 (a) and (b). It can be observed that they all exhibit Type IV isotherms (Fig. 4 (a) and (b)), indicating the presence of a mesoporous structure[33]. The specific surface areas of BCX, Fe@BCX, MFB and MFBX are 149.01, 151.42, 50.43 and 155.27 m^2/g. It can be seen that MFBX (155.27 m^2/g) has a larger surface area than BCX (149.01 m^2/g), as shown in Tables S5 and S6, indicating that loading BCX onto MFB increases its specific surface area. Furthermore, the corresponding pore diameter of MFBX (5.264 nm) is larger than that of BCX (4.201 nm). The increased specific surface area and larger pore size provide more sites for subsequent active substances and enhance mass transfer between these and the pollutants; it will also enhance the efficiency of MFBX/PS and MFBY/PS in degrading TPH.

Hysteresis loop testing is one of the simplest and most effective methods for separating and reusing magnetic catalysts. To this end, a variable-field saturation (VSM) test was conducted on the materials at room temperature[27]. Fig. 4c shows the superparamagnetic curves of MFB, MFBX and MFBY. The VSM curves indicate that MFB, MFBX and MFBY possess good magnetic properties, with saturation magnetizations of 50.16, 8.79 and 11.15 (emu/g), respectively. The reason for the relatively significant decrease in magnetic strength of MFBX and MFBY compared to MFB is attributed to the non-magnetic BC, which is consistent with previous studies[31]. It demonstrates that MFB has been successfully loaded onto the BC, and that MFBX and MFBY retain their magnetic properties. Under the influence of an external magnet, MFBX and MFBY can be rapidly separated, providing a loss-free and convenient method for the subsequent recycling and recovery of the catalyst.

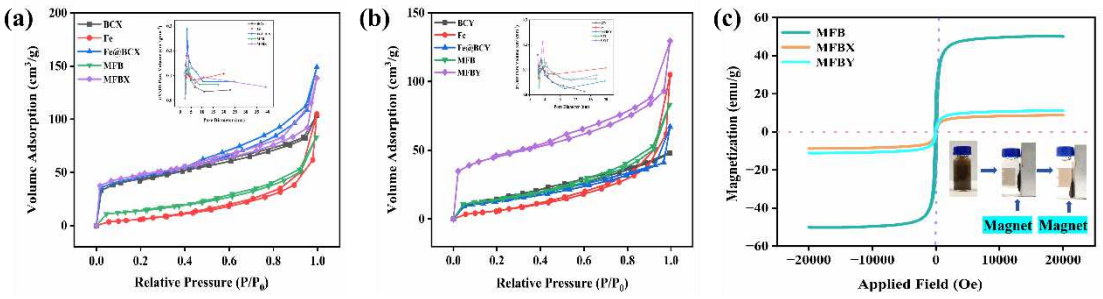


Fig. 4 (a), (b) and (c) show the N_2 adsorption–desorption isotherms and corresponding pore size distribution diagrams for wheat straw (inset) and hysteresis loops of MFBX and MFBY at room temperature, and the magnetic separation picture (inset) of MFBX and MFBY.

3.2 Degradation of TPH in wastewater by MFBX/PS and MFBY/PS

To determine the optimal conditions for MFBY/PS, the following parameter experiments were conducted to determine the optimal conditions for the degradation of TPH by MFBY/PS. Fig. 5 illustrates the effects of two types of biomass—corn cobs (BCY) and wheat straw (BCX)—on petroleum hydrocarbon degradation under varying iron-to-manganese ratios Fig. 5a, biochar dosages Fig. 5b, reaction times Fig. 5c, sodium persulfate concentrations Fig. 5d, different catalyst loading levels Fig. 5e and different catalysts sodium persulfate concentrations Fig. 5d, different catalyst loading levels Fig. 5e and different catalysts Fig. 5f. At a PS concentration of 15 mmol, the

effects of different ratios of Fe $(NO_3)_3 \cdot 9H_2O$ and Mn $(NO_3)_2 \cdot 4H_2O$ on the degradation efficiency of TPH were investigated. According to previous literature[32][34], BC has been widely used as a support material for various types of catalysts and has been shown to synergistically enhance their catalytic performance, and the characterization results mentioned above, indicate that MFB alone exhibits severe agglomeration and caking, whereas loading it onto a biochar carrier helps to suppress this caking; furthermore, the graphitic structure of biochar also facilitates electron transfer and the activation of PS[35-36]. Therefore, to fully utilize the dispersion function of the biochar carrier, it is essential to determine the optimal ratio of BC(X/Y) to MFB(X/Y)[27][37]. Fig. 5a shows the effect of different Fe $(NO_3)_3 \cdot 9H_2O$ and Mn $(NO_3)_2 \cdot 4H_2O$ ratios on the degradation efficiency of TPH. As shown in Fig. 5a, except for MFB(Y)-3:1 and 4:1, MFB with different mass ratios exhibits superior TPH degradation capacity compared to standalone MFB. When the ratio of Fe $(NO_3)_3 \cdot 9H_2O$ to Mn $(NO_3)_2 \cdot 4H_2O$ increased from 1:1 to 5:1, the TPH degradation rate of MFBX first increased from 62.61% to 84.44% and then decreased to 75.57%. The TPH degradation rate of MFBY increased from 74.55% to 88.05% before decreasing to 78.93%. As the ratio of $Mn(NO_3)_2 \cdot 4H_2O$ to $Fe(NO_3)_3 \cdot 9H_2O$ increased from 1:3 to 1: 4, the TPH degradation rates were all lower than when the ratio of $Fe(NO_3)_3 \cdot 9H_2O$ to $Mn(NO_3)_2 \cdot 4H_2O$ was 4:1. This preliminarily indicates that iron plays a dominant catalytic role in MFBX and MFBY. Excessive MFB in the catalyst increases the risk of metal leaching, which is harmful to the environment. Considering both reagent costs and TPH degradation efficiency, a 4:1 ratio of Fe $(NO_3)_3 \cdot 9H_2O$ to Mn $(NO_3)_2 \cdot 4H_2O$ was determined to be optimal and was used in subsequent experiments.

The effect of biomass dosage on the degradation efficiency of TPH was investigated at a fixed ratio of Fe $(NO_3)_3 \cdot 9H_2O$ to Mn $(NO_3)_2 \cdot 4H_2O$ of 4:1. As shown in Fig. 5b, as the BC dosage increased from 1 g to 10 g, the degradation of TPH initially increased and then decreased; however, for BCX and BCY, the maximum degradation rates were achieved at an addition of 5 g, at 84.44% and 88.05% respectively. This may be due to the organic matter on the biomass surface reacting with SO_4^{2-} and OH^-, thereby reducing the variety of active substances and increasing the contact area between PS

and TPH[38-39]. Observations of MFBX (d, e, f) and MFBY (i, j, k) in Fig. 4 reveal that when the amount of biochar added is excessive, agglomeration of biochar particles occurs. This may encapsulate active sites such as Fe and Mn, preventing them from binding with PS and TPH and consequently reducing the TPH degradation efficiency. In summary, it is determined that an addition of 5 g of biochar is the optimal amount.

With the ratio of Fe $(NO_3)_3 \cdot 9H_2O$ to Mn $(NO_3)_2 \cdot 4H_2O$ fixed at 4:1, the effect of reaction time on TPH degradation efficiency was investigated, as shown in Fig. 5c. As the reaction time increased from 12 h to 82 h, the TPH degradation rate first increased and then decreased, reaching the optimal degradation efficiency at 24 h. with degradation rates of 84.44% and 88.05% respectively. The fact that the TPH degradation rate declined after 24 h may be attributed to the continuous consumption of PS over time, causing the free radical concentration to peak and then drop rapidly, thereby eliminating the oxidative driving force. Furthermore, an imbalance in the redox cycles of iron and manganese ions (e.g., $Fe^{2+} \rightleftharpoons Fe^{3+}$, $Mn^{2+} \rightleftharpoons Mn^{3+}$) leads to a reduction in the number of catalytically active sites. Therefore, the optimal reaction time is determined to be 24 h.

Under conditions where the ratio of Fe $(NO_3)_3 \cdot 9H_2O$ to Mn $(NO_3)_2 \cdot 4H_2O$ was fixed at 4:1, the reaction time was 24 h, and the amount of BC added was 5 g, the effect of $Na_2S_2O_8$ concentration on the degradation of TPH was investigated in Fig.5d. As the concentration of $Na_2S_2O_8$ increased, the degradation rate of TPH by MFBX/PS rose from 31.45% to 84.44% before decreasing to 50.68%. The TPH degradation rate of MFBY/PS increased from 65.43% to 88.05% before eventually stabilizing at 66.75%. This may be attributed to the higher concentration of $Na_2S_2O_8$ providing a substantial amount of $S_2O_8^{2-}$ for the activation of Fe and Mn; the optimal effect was observed at a concentration of 15 mmol. Further increases actually led to a decrease in the TPH degradation rate, which may be attributed to the radical self-quenching effect between $HSO_5^{\bullet-}$ and SO_4^{2-}(through Eq. (5)-(6))[32][40].

$$HSO_5^- + SO_4^{\bullet-} \rightarrow HSO_5^{\bullet-} + SO_4^{2-} + H^+ \quad \text{Eq (5)}$$

$$SO_4^{\bullet-} + SO_4^{\bullet-} \rightarrow S_2O_8^{2-} \quad \text{Eq (6)}$$

Given a fixed ratio of Fe $(NO_3)_3 \cdot 9H_2O$ to Mn $(NO_3)_2 \cdot 4H_2O$ of 4:1, a reaction time of 24 h, a BC addition of 5 g, and a $Na_2S_2O_8$ concentration of 15 mmol, the effect of MFBX and MFBY dosages on TPH degradation was investigated in Fig.5e. As the dosages of MFBX and MFBY increased, the TPH degradation rate of MFBX/PS rose from 37.08% to 84.44%; however, upon further increasing the MFBX dosage, the TPH degradation rate actually decreased to 72.57%, the degradation rate of TPH by MFBY/PS rose from 45.06% to 88.05%, before eventually falling to 78.12%, It may be that, as the amount of catalyst increases, so does the amount of active material; once the active material reaches saturation, any further increase in the catalyst causes the radicals to undergo self-quenching and react with high concentrations of Fe^{3+} and • OH, thereby reducing the concentration and efficiency of the effective oxygen.

At a fixed PS concentration of 15 mmol and a catalyst loading of 0.5 g, the effect of different catalysts—Fe powder, Mn, Fe, BCX, FBX, FMB, MFBCX, BCY, FBY and MFBY—on the degradation of TPH was investigated. Fig. 5f shows the degradation of TPH at a fixed PS concentration. Here, the degradation rates of TPH by BCX and BCY alone are higher than those of Fe, whilst Fe@BCX and Fe@BCY are higher than BCX and BCY, respectively. This may be due to the enrichment effect of BCX/Y on TPH, whereas the reaction between Fe and PS alone results in a lower degradation efficiency than the adsorption by BCX/Y alone. However, the degradation efficiency of Fe@BCX/Y-activated PS towards TPH outperforms that of standalone BCX/Y and Fe, indicating that Fe@BCX/Y-activated PS exhibits a synergistic effect of adsorption and catalytic degradation[10]. The subsequent addition of manganese further enhanced the degradation efficiency of TPH, with the degradation efficiency increasing from 75.65% to 84.44% and 88.05%, consequently, the combination of bimetal and BC not only provides more active sites for PS activation but also generates a synergistic effect that promotes PS activation. This, in turn, enhances the degradation of TPH[27].

Similar studies have investigated the adsorption capacity of TPH at different initial concentrations of 500, 1000, 5000, and 10,000 mg/L. As shown in Figs. S1 and S2 and Tables S7 and S8, adsorption reached a steady state after 20 h for initial concentrations

of 500, 1000, and 5000 mg/L, with an adsorption rate of 49.13%, whilst adsorption stabilized after 24 h for 10,000 mg/L, with an adsorption rate of 50.12%. Regarding the adsorption behavior, it was found that regardless of the TPH concentration, the R^2value for the pseudo-first-order kinetic model of BCX was greater than that of the pseudo-second-order kinetic model, making it a better fit for the pseudo-first-order model. Conversely, for MFBX adsorption, the R^2value for the pseudo-second-order kinetic model was greater than that of the pseudo-first-order model, making it a better fit for the pseudo-second-order model. Overall, $MFBX_{4:1}$-5 still exhibits good adsorption performance across a wide range of TPH concentrations. This lays the foundation for subsequent selection and utilization at a concentration of 1000 mg/L.

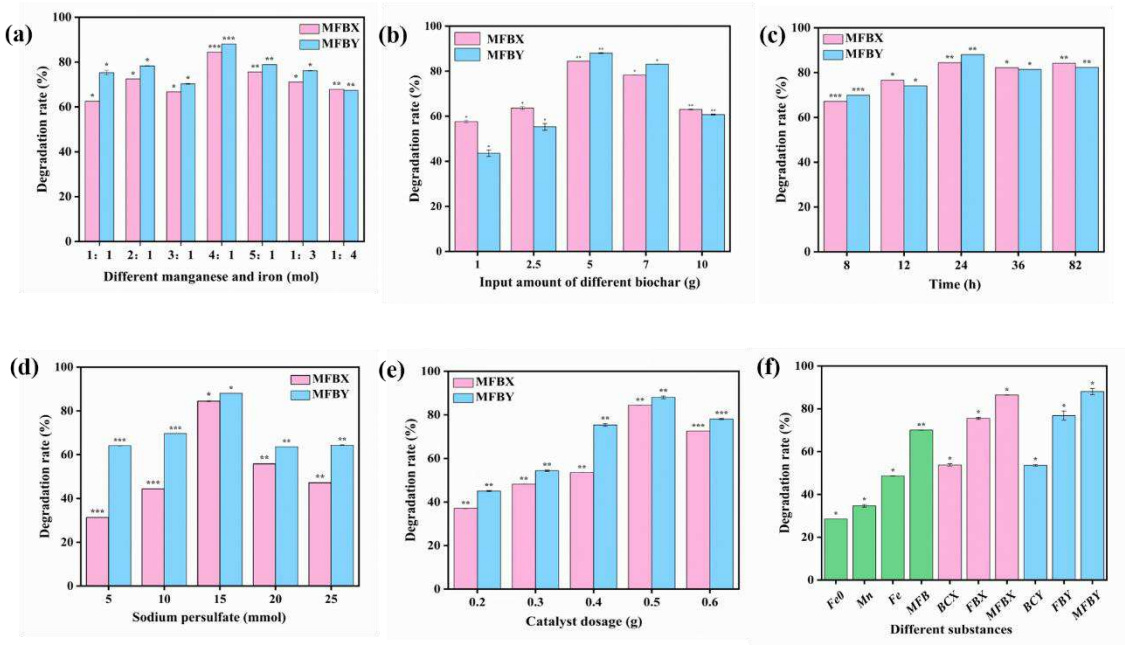


Fig. 6 (a), (b), (c), (d) and (e) examine the effects of two types of biomasses—maize cobs (BCY) and wheat straw (BCX)—on the degradation of TPH in the $MnFe_2O_4$@BC/PS system and different catalysts (f) under different iron-to-manganese ratios (a), different biochar dosages (b), different time intervals (c), different PS concentrations (d) and different catalyst dosages (e)

3.4 Possible mechanisms of TPH degradation

3.4.1 Identification of reactive oxygen species

Previous studies have identified $SO_4^{\bullet-}$, •OH, $^1O_2$, and $O_2^{\bullet-}$ as the primary reactive oxygen species in PS systems[2][41-42]. To determine which reactive oxygen species play

a significant role in the $MnFe_2O_4$@BC/PS, MFBX/PS, and MFBY/PS systems, quenching experiments were conducted using the corresponding chemical quenchers EtOH, TBA, BQ, and FFA to quench $SO_4^{\bullet-}$, •OH, $^1O_2$, and $O_2^{\bullet-}$. The results are shown in Fig. 7[27]. As observed in Figs. 7(a) and 7(b), after adding the four quenchers—EtOH, TBA, BQ, and FFA, the degradation rates of TPH in the wastewater were 54.29%, 43.7%, 13.42%, and 22.38%, and 46.75%, 34.15%, 16.54%, and 28.64%, respectively. This indicates that during the degradation process, $SO_4^{\bullet-}$and •OH made a significant contribution in the $MnFe_2O_4$@BCX/PS and $MnFe_2O_4$@BCY/PS systems, whilst $^1O_2$ and $O_2^{\bullet-}$ had a limited effect on TPH[43]. However, the addition of $^1O_2$ and $O_2^{\bullet-}$ still resulted in a certain degree of TPH degradation; according to previous studies[2][44], $SO_4^{\bullet-}$ is the primary active radical in the $MnFe_2O_4$@BCX/PS and $MnFe_2O_4$@BCY/PS systems, whilst $O_2^{\bullet-}$ is an inactive radical. We therefore speculate that this may be due to the $MnFe_2O_4$@BC composites being more prone to generating $O_2^{\bullet-}$ and $^1O_2$ in subsequent degradation reactions. $O_2^{\bullet-}$ can be generated via electron transfer from O_2, and the standard redox potentials of O_2/ $O_2^{\bullet-}$ and Fe(III)/Fe(II) in aqueous solution are −0.33 V and 0.77 V, respectively, which is thermodynamically feasible[27-28][45]. It can thus be seen that $O_2^{\bullet-}$ not only participates in the Fe (II)/Fe (III) cycle, but also in the process of PS activation to generate $SO_4^{\bullet-}$. Studies have shown that $^1O_2$ also contributes to the degradation and mineralization of organic pollutants [2][46].

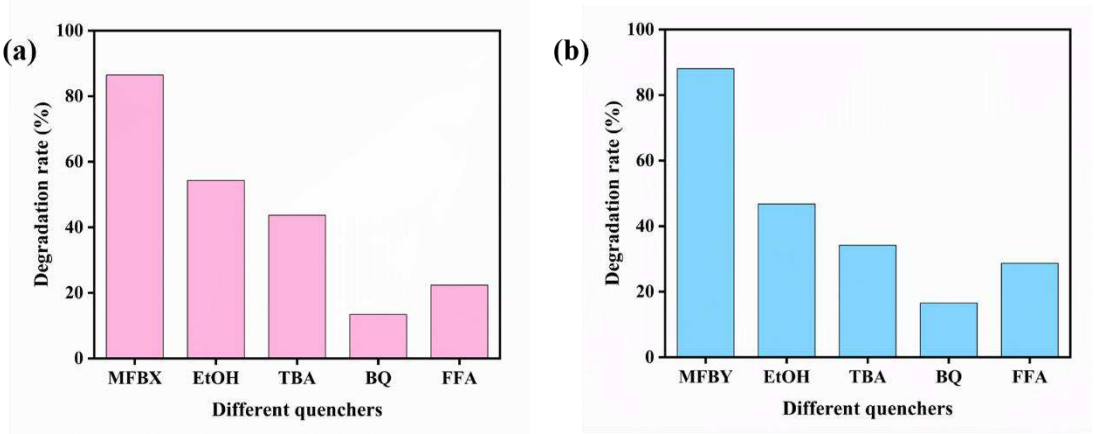


Fig. 7 Radical scavenging by ethanol, TBA, BQ and FFA (reaction conditions: TPH = 1000 mg/L, PS = 15 mmol, MFBX/Y = 0.5 g, T = 25.00 ± 1 °C, initial pH not adjusted, ethanol or tert-butyl alcohol/PS = 500:1, BQ or FFA/PS = 300:1)

3.4.2 Valence state changes and synergy of Fe-Mn bimetals

To investigate the metal valence states on the surfaces of the MFBX and MFBY catalysts and analyse their interaction with the transition metals, XPS was employed to analyse the spectra of fresh and spent MFBX and MFBY, as shown in Fig. 8. The full-size XPS spectra of the MFBX and MFBY composites before and after the reaction, as shown in Fig. 8, exhibit four peaks: C1s, O1s, Fe2p and Mn2p, as illustrated in Fig. 8 (a) and (e). After 24 h of reaction, it was observed that there was little change in the surface elements of both the fresh and used catalysts, indicating that the MFBX and MFBY catalysts possess relative stability. As shown in Fig. 8 (b) and (f), the C1s peaks at 283.5, 284.8 and 287.8 (eV) correspond to C=C/C-C, C-O and C=O bonds, whilst those at 284.2 and 284.9 (eV) correspond to C=C/C–C, C–O and C=O bonds, indicating that carbon participates in a variety of bonding modes within the material; as shown in Figs. 8 (c) and (d), the two asymmetric doublets in the Fe 2p spectra of the MFBX composite at 710.5 and 713.5 (eV) correspond to Fe $2p_{3/2}$ and Fe $2p_{1/2}$, respectively. The peaks at 710.3 and 723.6 (eV) correspond to Fe 2p 3/2 and Fe 2p 1/2, respectively, both of which are associated with Fe (II), whilst those at 713.4 and 726.3 (eV) correspond to Fe 2p 3/2 and Fe 2p 1/2, respectively, both of which are associated with Fe (III). With the use of the catalytic material, as shown in Tables S9 and S10, following the degradation experiment, the percentage content of Fe (II) increased from (45.5%) to (65.48%), whilst that of Fe (III) decreased from (54.5%) to (34.52%). In Mn, peaks at 640.1, 641.9, 650.8 and 653.2 (eV) correspond to Mn 2p3/2, at 645.8 and 656.9 (eV) to Mn 2p1/2, and 640.5, 641.7, 650.6 and 654.2 are all associated with Mn (II) and Mn (III), whilst 644.8 and 656.4 are both associated with Mn (IV). As the catalytic material activates PS for the degradation of TPH, the percentage of Mn (II) increases from (43.14%) to (48.22%), the percentage of Mn (III) decreases from (45.38%) to (36.14%), whilst the percentage of Mn (IV) increased from (11.48%) to (15.64%). Similarly, in the MFBY samples shown in (g) and (h), the Fe 2p 3/2 and Fe 2p 1/2 lines in MFBY correspond to 709.4 and 712.1 (eV). 709.6 and 722.8 (eV) correspond to Fe $2p_{3/2}$ and Fe $2p_{1/2}$, respectively, both of which are associated with Fe (II), whilst 712.1 and 725.4

(eV) correspond to Fe $2p_{3/2}$ and Fe $2p_{1/2}$, respectively, both of which are associated with Fe (III), and there is a satellite peak at 717.4 (eV). following the use of the catalytic material, the percentage content of Fe(II) decreased from (57.86%) to (53.03%) and that of Fe(III) from (42.14%) to (46.97%) after the degradation experiment; furthermore, in the Mn metal, peaks were observed at 639.4, 641.4 and 650.3, 652.2 eV correspond to Mn 2p3/2, whilst 645.4 and 656.4 eV correspond to Mn 2p1/2; furthermore, the peaks at 640.0, 642.3 and 650.2, 653.3 (eV) are all associated with Mn(II) and Mn(III), whilst 645.3 and 656.3 (eV) are both associated with Mn(IV). Furthermore, the percentage of Mn(II) increased from (50.21%) to (54.17%), the percentage of Mn(III) decreased from (36.36%) to (35.55%), and the percentage of Mn(IV) decreased from (13.43%) to (10.27%), Based on the changes in the valence states of these two metals, it can be seen that Fe(III) and Mn(II) are partially converted to Mn(II) and Fe(II) on the surface of the $MnFe_2O_4$@BC composite; consequently, the Mn(II)/Mn(II) and Fe(III)/Fe(II) cycles participate in the catalytic system. Previous studies have shown that Mn (II)/Mn (II) and Fe (III)/Fe (II) can undergo multiplication reactions with PS and the generated radicals, ensuring the continuous generation of radicals. This result also supports the excellent reusability of the MFBX and MFBY catalysts. Given the difficulty in reducing Fe (III) in iron-based catalysts, high-resolution Fe 2p and Mn 2p spectra, along with changes in the relative abundances of Fe and Mn species, confirm the synergistic effect of the Fe-Mn bimetallic system. This enables the cycling of Mn (II)/Mn (II) and Fe (III)/Fe (II), further indicating charge transfer between Fe and Mn. The synergistic effect of the iron-manganese bimetallic system is a key factor in activating PS for the degradation of TPH.

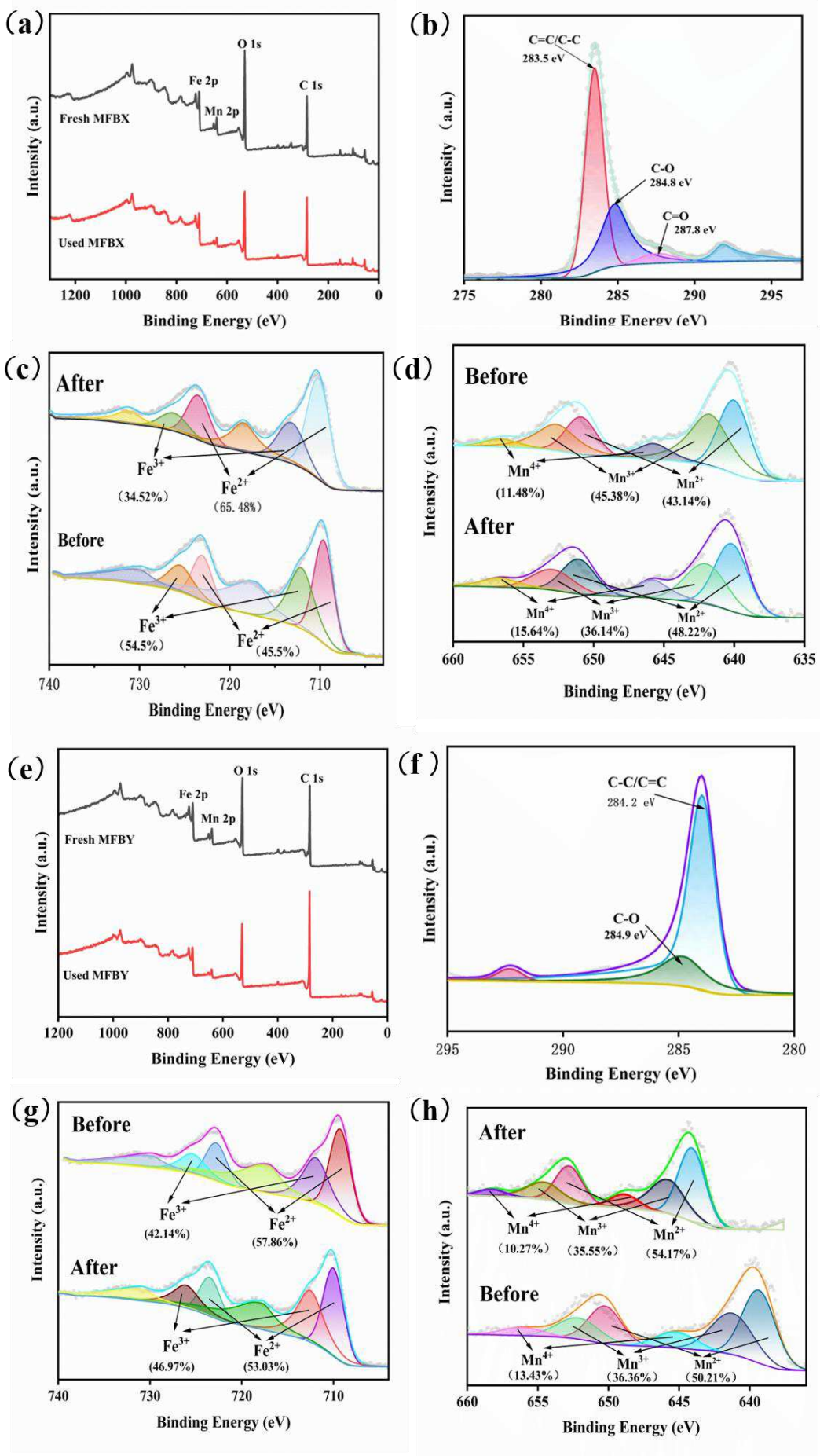

(a)
O 1s
Fe 2p
Mn 2p
C 1s
Fresh MFBX
Used MFBX
Intensity (a.u.)
1200 1000 800 600 400 200 0
Binding Energy (eV)
(b)
C=C/C-C
283.5 eV
C-O
284.8 eV
C=O
287.8 eV
Intensity (a.u.)
275 280 285 290 295
Binding Energy (eV)
(c)
After
Fe3+
(34.52%)
Fe2+
(65.48%)
Before
Fe3+
(54.5%)
Fe2+
(45.5%)
Intensity (a.u.)
740 730 720 710
Binding Energy (eV)
(d)
Before
Mn4+
(11.48%)
Mn3+
(45.38%)
Mn2+
(43.14%)
After
Mn4+
(15.64%)
Mn3+
(36.14%)
Mn2+
(48.22%)
Intensity (a.u.)
660 655 650 645 640 635
Binding Energy (eV)
(e)
O 1s
Fe 2p
Mn 2p
C 1s
Fresh MFBY
Used MFBY
Intensity (a.u.)
1200 1000 800 600 400 200 0
Binding Energy (eV)
(f)
C-C/C=C
284.2 eV
C-O
284.9 eV
Intensity (a.u.)
295 290 285 280
Binding Energy (eV)
(g)
Before
Fe3+
(42.14%)
Fe2+
(57.86%)
After
Fe3+
(46.97%)
Fe2+
(53.03%)
Intensity (a.u.)
740 730 720 710
Binding Energy (eV)
(h)
After
Mn4+
(10.27%)
Mn3+
(35.55%)
Mn2+
(54.17%)
Before
Mn4+
(13.43%)
Mn3+
(36.36%)
Mn2+
(50.21%)
Intensity (a.u.)
660 655 650 645 640
Binding Energy (eV)

Fig. 8 XPS spectra of fresh and used MFBX and MFBY composites: (a) MFBX overall, (b) C 1s, (c) Fe 2p, (d) Mn 2p; (f) MFBY overall, (e) C 1s, (f) Fe 2p, (g) Mn 2p

3.4.3 Mechanism of PS activation by MFB (X, Y)

Generally, the production of $^1O_2$ in the premenstrual syndrome system is considered to be a non-radical pathway[27][47]. In addition to $^1O_2$, electron transfer and surface-activated complex mechanisms represent two further non-radical pathways. According to our previous studies, high-temperature pyrolysis increases the degree of graphitization in BC, which is conducive to electron transfer (e.g., at 700°C); the porous structure of BC may play a significant role in the activated degradation of pollutants by PS [42]. Based on the above results and discussion, it can be reasonably inferred that in the degradation of TPH by the two systems, $MnFe_2O_4$@BCX/PS and $MnFe_2O_4$@BCY/PS, the relationship between radical and non-radical mechanisms involves the coexistence of radicals ($SO_4^{\bullet-}$, •OH, $O_2^{\bullet-}$) and non-radical mechanisms ($^1O_2$ and electron transfer), with the activation mechanism illustrated in Fig. 9.

Firstly, the Fe- and Mn-enriched zones of the $MnFe_2O_4$@BC material serve as the primary catalytic centers for the activation of PS. The experiments described above demonstrated that Fe and Mn exhibit a synergistic effect; when PS comes into contact with $MnFe_2O_4$@BC via electrostatic attraction, it interacts with the active sites of Fe (II), Fe (III), Mn (II), Mn (III) and Mn (IV) at the active sites of $MnFe_2O_4$@BC, Mn (II) and Fe (III) interconvert to form Mn (III) and Fe (II) (Eq.(7)). This cycle provides the activation of $S_2O_8^{2-}$ via the Fe (II), Mn (II) and Mn (III) centers to generate $SO_4^{\bullet-}$, SO_4^{2-}, as well as the corresponding Fe (III), Mn (III) and Mn (IV). (Eqs. (8)–(10)) Based on the changes in Fe and Mn content in $MnFe_2O_4$@BC described above (Eqs.(7)–(10)), it can be deduced that $SO_4^{\bullet-}$ reacts with H_2O or OH^- to produce SO_4^{2-} and •OH [43]. (Eqs. (11) and (12))

Secondly, the phenolic hydroxyl groups (Ar-OH) on the surface of biochar act as a continuous electron source within the system; they can therefore react with OH^- to form Ar-O^-, which in turn reacts with Fe(III), Mn(III) and Mn(IV) centers to generate the corresponding lower-valent Fe(II) and Mn(II) species, as well as $O_2^{\bullet-}$, (Eqs.(13)–(16))

Simultaneously, at specific sites on the interface, Fe(II) and Mn(II) can also react directly with O_2 to form Fe(III) and Mn(III) with $O_2^{\bullet-}$, (Eqs.(17)–(18)) whilst PS undergoes hydrolysis and activation by alkali to generate $O_2^{\bullet-}$, $S_2O_8^{2-}$ (Eqs.(19)–(21)), whilst $O_2^{\bullet-}$ acts as a reducing agent to reduce Fe(III) and Mn(III) to Fe(II) and Mn(II) in the presence of O_2, (Eqs.(22)–(24)) thereby providing the material cycle for the preceding reactions (Eqs.(13)–(21)). As the most central non-radical active species in this system, $O_2^{\bullet-}$ hydrolyses to form $^1O_2$, OH^- and H_2O_2. The metastable manganese intermediate of Mn(IV) can combine with the generated $O_2^{\bullet-}$ to form $^1O_2$, or it can be converted into $^1O_2$ through reactions with HSO_5^- and $O_2^{\bullet-}$[29][48]. (Eqs.(25)–(30)) More importantly, the results of the aforementioned data indicate that iron and manganese in this system are more inclined to activate PS to generate $O_2^{\bullet-}$ and $^1O_2$ [2][49]. Therefore, it is boldly speculated that this may be the result of synergistic interaction between BC and $MnFe_2O_4$. Furthermore, high-temperature pyrolysis of BC facilitates electron transfer, and the porous structure of BC may also play a significant role in the activation of PS for the degradation of pollutants.

Finally, all the free radicals react with TPH, leading to the degradation of the pollutant into CO_2 and H_2O(Eq.(31))[27][50-51].

$$\equiv Mn\ (II) + Fe\ (III) \rightarrow Mn\ (III) + Fe\ (II) \quad (7)$$

$$\equiv Mn\ (II) + S_2O_8^{2-} \rightarrow Mn\ (III) + SO_4^{\bullet-} + SO_4^{2-} \quad (8)$$

$$\equiv Mn\ (III) + S_2O_8^{2-} \rightarrow Mn\ (IV) + SO_4^{\bullet-} + SO_4^{2-} \quad (9)$$

$$\equiv Fe\ (II) + S_2O_8^{2-} \rightarrow Fe\ (III) + SO_4^{\bullet-} + SO_4^{2-} \quad (10)$$

$$SO_4^{\bullet-} + H_2O \rightarrow SO_4^{2-} + \bullet OH + H^+ \quad (11)$$

$$SO_4^{\bullet-} + OH^- \rightarrow SO_4^{2-} + \bullet OH \quad (12)$$

$$Ar\text{-}OH + OH^- \rightarrow Ar\text{-}O^- + H_2O \quad (13)$$

$$Ar\text{-}O^- + \equiv Fe\ (III) + O_2 \rightarrow Ar\text{-}O\cdot + \equiv Fe\ (II) + O_2^{\bullet-} \quad (14)$$

$$Ar\text{-}O^{-}+\equiv Mn\ (III)+O_2\rightarrow Ar\text{-}O\cdot+\equiv Mn\ (II)+O_2^{\bullet-} \quad (15)$$

$$2Ar\text{-}O^{-}+Mn\ (IV)+2O_2\rightarrow 2Ar\text{-}O\cdot+\equiv Mn\ (II)+2O_2^{\bullet-} \quad (16)$$

$$\equiv Fe\ (II)+O_2\rightarrow\equiv Fe\ (III)+O_2^{\bullet-} \quad (17)$$

$$\equiv Mn\ (II)+O_2\rightarrow Mn\ (III)+O_2^{\bullet-} \quad (19)$$

$$S_2O_8^{2-}+H_2O\rightarrow HSO_5^{-}+HSO_4^{-} \quad (20)$$

$$HSO_5^{-}+OH^{-}\rightarrow SO_5^{2-}+H_2O \quad (21)$$

$$2SO_5^{2-}+H_2O\rightarrow 2SO_4^{2-}+2H^{+}+O_2^{\bullet-} \quad (22)$$

$$\equiv Fe\ (III)+O_2^{\bullet-}\rightarrow\equiv Fe\ (II)+O_2 \quad (23)$$

$$\equiv Mn\ (III)+O_2^{\bullet-}\rightarrow\equiv Mn\ (II)+O_2 \quad (24)$$

$$\equiv Mn\ (IV)+2O_2^{\bullet-}\rightarrow\equiv Mn\ (II)+2O_2 \quad (25)$$

$$2O_2^{\bullet-}+2H_2O\rightarrow {}^1O_2+H_2O_2+2OH^{-} \quad (26)$$

$$\equiv Mn\ (IV)+S_2O_8^{2-}\rightarrow\equiv Mn\ (IV)\text{-}OOSO_3^{-}+SO_4^{2-} \quad (27)$$

$$\equiv Mn\ (IV)\text{-}OOSO_3^{-}+H_2O\rightarrow\equiv Mn\ (III)+SO_4^{2-}+SO_5^{\bullet-}+2H^{+} \quad (28)$$

$$2SO_5^{\bullet-}\rightarrow 2SO_4^{2-}+2H^{+}+{}^1O_2 \quad (29)$$

$$2HSO_5^{-}\rightarrow 2HSO_4^{-}+{}^1O_2 \quad (30)$$

$$SO_4^{\bullet-}/\bullet OH/{}^1O_2/O_2^{\bullet-}+TPH\rightarrow intermediates\rightarrow CO_2+H_2O \quad (31)$$

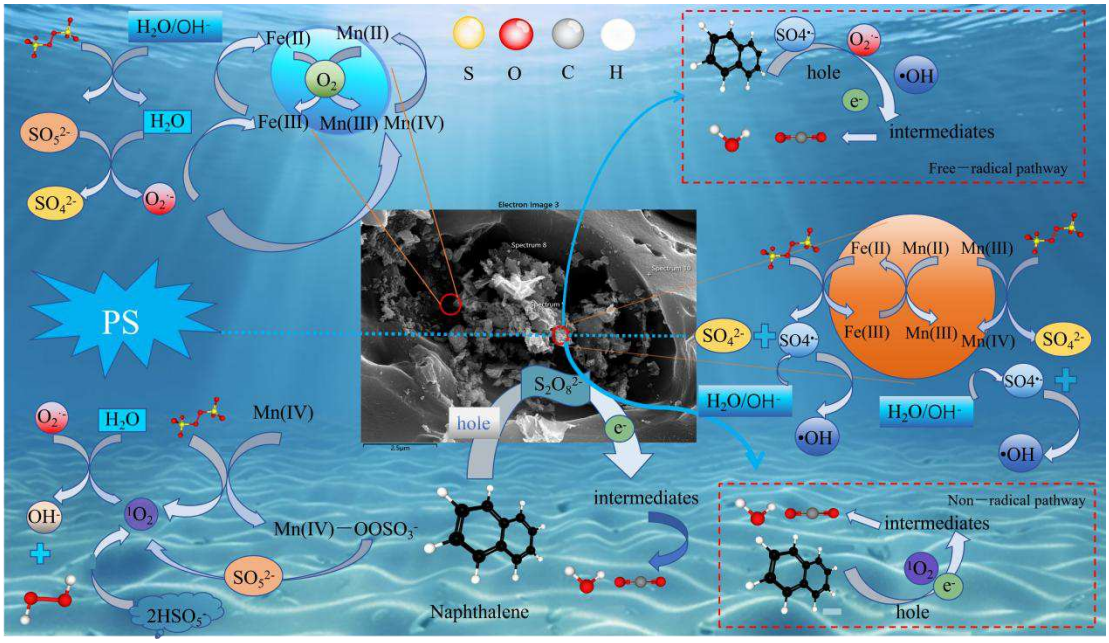


Fig. 9 Mechanism of TPH degradation by $MnFe_2O_4$@BC/PS

3.4.4 Degradation pathways of TPH in the $MnFe_2O_4$@BCX/Y system

To gain a better understanding of the catalytic degradation pathways of MFBX/Y, possible degradation pathways were proposed. Using GC analysis, the degradation intermediates of MFBX/Y for naphthalene—a representative petroleum hydrocarbon—were determined. Fig. 10 illustrates the possible degradation pathways of MFBX/Y for naphthalene. It was found that the radical $SO_4^{\bullet -}$ and •OH attack the α-position to form -OH at the α-site (P1), which is further oxidized to yield 1,4-naphthoquinone (P2), whilst $^1O_2$ attacks directly via a non-radical mechanism and undergoes oxidation with its own intermediate to yield 1,4-naphthoquinone (P2). This occurs preferentially on aromatic rings modified by unionization or hydroxylation, breaking non-conjugated C-C bonds at the 1-2, 3–4 (or 5–6, 7–8) non-conjugated C–C bonds; some intermediates may undergo concomitant cleavage of the C4–4a bond, thereby generating intermediates such as phthalic acid (P5), benzoic acid (P6), and (P7)[51]. Concurrently, the synergistic effect of MFB adsorption and in-situ oxidation allows naphthalene to be concentrated on the catalyst surface; the high-concentration ROS generated in situ can rapidly complete the consecutive reactions of hydroxylation and ring-opening, thereby preventing the reverse reaction of intermediates and significantly enhancing the ring-

opening efficiency; the Fe-Mn valence state cycle ensures a continuous supply of ROS, enabling the ring-opening reaction to proceed efficiently even under neutral or weakly basic conditions. Subsequently, phthalic acid (P5), benzoic acid (P6), and others undergo hydroxylation of the benzene ring first, generating polyhydroxy benzene derivatives such as o-hydroquinone (P8) and p-hydroquinone (P9) [52-53], which activate the benzene ring structure. Ring-opening then occurs at the ortho position, breaking the C–C bond adjacent to the two hydroxyl groups on the benzene ring to generate maleic acid (P10), fumaric acid (P11), acrylic acid (P12) and other unsaturated fatty acids, which are further oxidized to oxalic acid (P13), formic acid (P14), acetic acid (P12) and other saturated small-molecule carboxylic acids. Finally, the small-molecule fatty carboxylic acids are continuously oxidized by ROS within the system, ultimately being completely mineralized into CO_2 and H_2O[54-55].

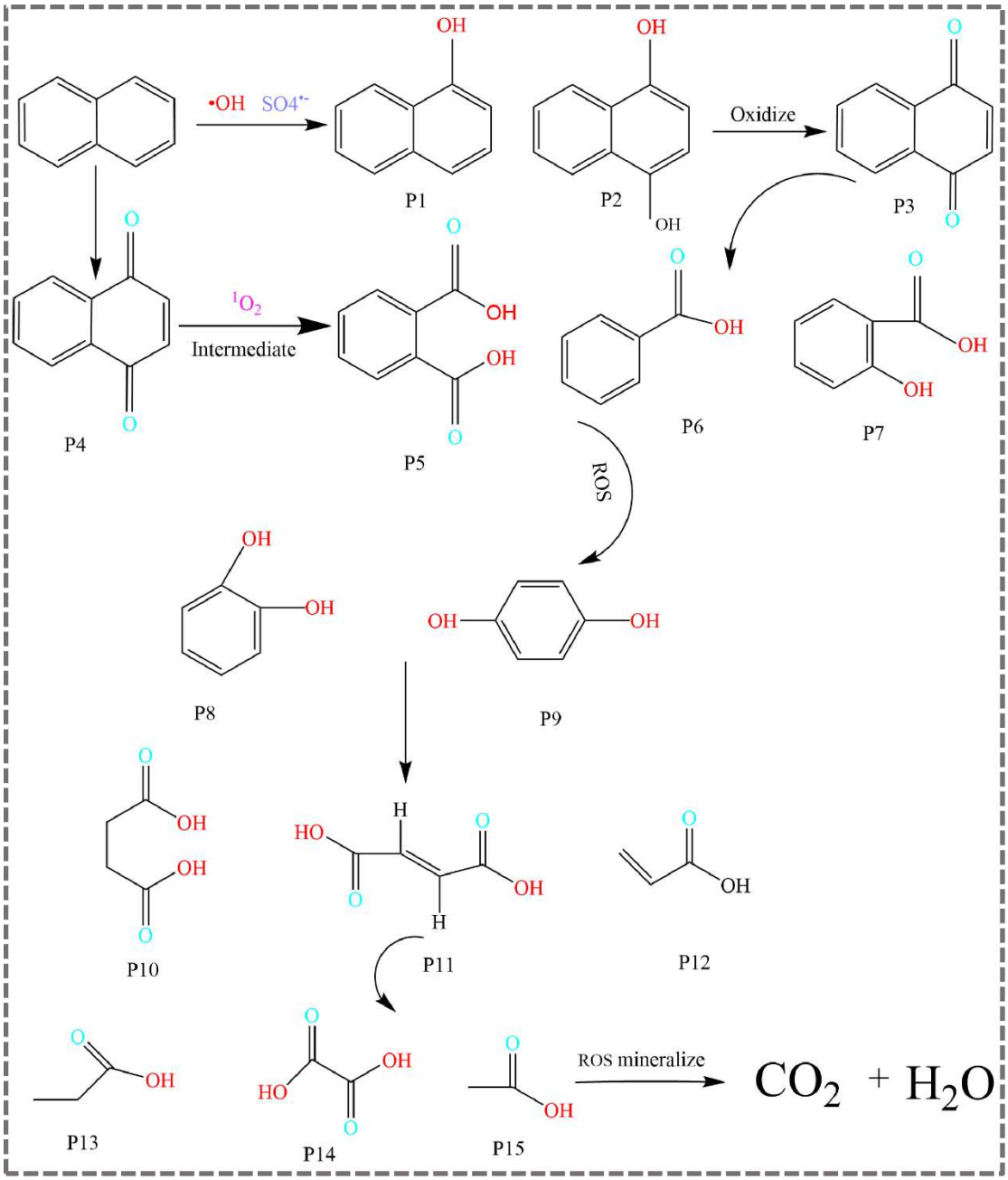


Fig. 10 Degradation pathways of TPH in the $MnFe_2O_4$@BCX/Y/PS system (reaction conditions: [TPH] = 1000 mg/L, [PS] = 15 mmol, [$MnFe_2O_4$@BCX/Y] = 0.5 g, T = 25 ± 1 °C, initial pH not adjusted).

3.5 Stability of the $MnFe_2O_4$@BCX/Y system and reproducibility of the composite material

For the practical application of the reaction system, the stability of both the system itself and the $MnFe_2O_4$@BCX/Y material is of paramount importance. Upon completion of the experiment, the catalyst was recovered using a magnet, rinsed, and dried at 50 °C

for 10 h for use in the next round of experiments, following the procedure described in Section 2.4. It was found that after five cycles, the degradation rates of MFBY and MFBX decreased from 84.44% and 88.05% to 76.56% and 79.46%, respectively, representing decreases of only 7.88% and 8.59%, respectively; therefore, the catalyst exhibits good stability and reusability in Fig.11(a) and (b)[55]. In degradation experiments, metal leaching can influence environmental risk assessments. To evaluate the stability of MFBY and MFBX composites during TPH degradation, the leaching of Fe and Mn was measured during the TPH degradation process with the addition of 0.5 g of catalyst (Fig.11c). After 24 h of reaction, the leaching levels of Fe and Mn corresponding to MFBX and MFBY were 118.977 (μg/L), 108.383 (μg/L), 48.131 (μg /L) and 46.236 (μg/L), respectively. Under normal circumstances, such concentrations do not pose a threat to the environment, thereby demonstrating that the $MnFe_2O_4$@BCX/Y catalyst possesses relatively good stability[56-57].

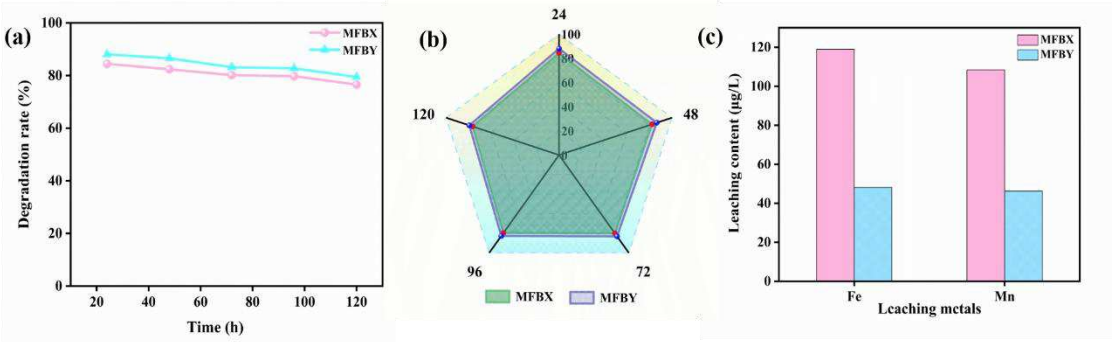


Fig. 11 Cycle test on the degradation of total petroleum hydrocarbons (TPH) by $MnFe_2O_4$@BC/PS. (a) and (b) Leaching concentrations of heavy metals 24 h after the reaction; (c)

4 Conclusions

In this study, the $MnFe_2O_4$@BCX/Y catalyst for PS activation was prepared using the sol-gel method. A heterogeneous persulphate activation system was established, and its effectiveness in degrading TPH was investigated. The results indicate that, based on various preparation parameters and reaction conditions, the optimal conditions—achieved at a Fe: Mn molar ratio of 4:1, a catalyst loading of 0.5 g, and a PS concentration of 15 mmol—resulted in a reaction time of 24 h, yielding maximum TPH degradation rates of 84.44% and 88.05%, respectively. Through quenching experiments

and characterization methods such as GC and XPS, it was found that the $MnFe_2O_4$@BCX/Y/PS system involves both radical and non-radical reaction pathways, with the radical pathway primarily dominated by $SO_4^{\bullet-}$, •OH, and $O_2^{\bullet-}$ and a non-radical pathway dominated by $^1O_2$. The redox interactions between Fe (III)/Mn (II) and Mn (II), as well as between Mn (III) and Mn (IV), together with the oxidizing species on the catalyst surface, enhance the generation of $SO_4^{\bullet-}$, • OH, $O_2^{\bullet-}$ and $^1O_2$—thereby promoting the degradation of TPH. The MFBY catalyst continued to exhibit excellent activation performance and good adaptability to the degradation of organic pollutants in water by activated PS even after four cycles, and a self-sustaining reaction mechanism was established within the system. This work provides a new approach for the design and preparation of Fe-Mn-based catalysts with high degradation performance.

Declaration of Competing Interests

The authors declare that they have no known competing financial interests or personal relationships that could have appeared to influence the work reported in this paper.

References

[1] Li, Yong-Tao, Qin Sui, Xi Li, et al. Enhanced In-Situ Zero-Valent Iron Activated Persulfate Oxidation with Electrokinetic for the Remediation of Petroleum Hydrocarbon Contaminated Soil. Journal of Environmental Chemical Engineering 12, 5 (2024),113781. https://doi.org/10.1016/j.jece.2024.113781

[2] Liu, Jia, Wen-Yan Li, Hong-Xin Chen, et al. Applications of Functional Nanoparticle–Stabilized Surfactant Foam in Petroleum-Contaminated Soil Remediation. Journal of Hazardous Materials 443 (February 2023), 130267. https://doi.org/10.1016/j.jhazmat.2022.130267

[3] Luo, Hu, Hao Wang, Ling Zhao Kong, Shen gang Li and Yuhan Sun. Insights into Oil Recovery, Soil Rehabilitation and Low Temperature Behaviors of Microwave-Assisted Petroleum-Contaminated Soil Remediation. Journal of Hazardous Materials 377 (2019): 341 ~ 48.

https://doi.org/10.1016/j.jhazmat.2019.05.092

[4] Hemati, Sara, Mohsen Heidari, Fariborz Momenbeik, et al. Co-Occurrence of Polycyclic Aromatic Hydrocarbons and Heavy Metals in Various Environmental Matrices of a Chronic Petroleum Polluted Region in Iran; Pollution Characterization, and Assessment of Ecological and Human Health Risks. Journal of Hazardous Materials 478 (October 2024): 135504. https://doi.org/10.1016/j.jhazmat.2024.135504

[5] Feizi, Rozhan, Iman Parseh, Ali Zafarzadeh, Sahand Jorfi, Amir Sheikhmohammadi. Optimizing a Hybrid Process of Electrolysis Ultrasound and Persulfate for Remediation of Petroleum Contaminated Soils Using AI Models. Scientific Reports 15, designated time 1 (2025): 22555. https://doi.org/10.1038/s41598-025-06819-8

[6] Ronghai Zhang, Yudao Chen, Shudi Li, Zhuangmian Wei, He Huang, Tian Xie, Remediation and optimization of petroleum hydrocarbon degradation in contaminated water by persulfate activated with bagasse biochar-supported nanoscale zerovalent iron. J Sustainability.14 (2022).9324.https://doi.org/10.3390/su14159324

[7] Chen L, Zuo X, Zhou L, et al. Efficient heterogeneous activation of peroxymonosulfate by facilely prepared Co/Fe bimetallic oxides: Kinetics and mechanism [J]. Chemical Engineering Journal, 2018,345: https://doi.org/10.1016/j.cej.2018.03.169

[8] Jin Zheng, Chunyang Gao, Xianyuan Du, Hongkun Chen ed al, Synthesis of iron-manganese bimetallic materials supported by activated carbon and application of activated persulfate in the degradation of soil contaminated by crude oil. J Environmental Research.258 (2024).119455. https://doi.org/10.1016/j.envres.2024.119455

[9] Cheng-Gang Niu, Hai Guo, Huai-Yuan Niu, Song Liang.Chao Liang, Hui-Yun Liu, Anchoring $CuFe_2O_4$ nanoparticles into N-doped carbon nanosheets for peroxymonosulfate activation: Built-in electric field dominated radical and non-radical process, Chem. End. [J]. Chemical Engineering Journal.426 (2021),130850. https://doi.org/10.1016/j.cej.2021.130850

[10] Wang H, Liu H, Chu Z, et.al. Fe_3O_4 derived from the decomposition of siderite as a heterogeneous photocatalyst to degrade 2,4-dichlorophenol via activating PMS[J]. Journal of Water Process Engineering, 2024, 57: 104538. https://doi.org/10.1016/j.jwpe.2023.104538

[11] L. J., Yong-Tao, Yu-Qin Wang, Xi Li, et al. Remediation of Petroleum Hydrocarbon

Contaminated Soils by NZVI Coupled with Electrokinetic Activation of Persulfate. Journal of Cleaner Production 459 (June 2024): 142514. https://doi.org/10.1016/j.jclepro.2024.142514

[12] Dong Meiling, Yang Hui, Liu Yuzheng. Research progress on advanced oxidation technology based on persulfate [J]. Liaoning Chemical Industry, 2024, 53 (08): 1285-1287. https://doi.org/10.14029/j.cnki.issn1004-0935.2024.08.038

[13] Wang X, Zhang C, Ma Y, et al. Readily separable and stable $CoFe_2O_4$ beads for activating peroxymonosulfate to degrade lomefloxacin hydrochloride: Optimization, performance and degradation mechanism [J]. Separation and Purification Technology, 2023, 327: 1249. https://doi.org/10.1016/j.seppur.2023.124975

[14] Wang C, Zhao J, Chen C, et al. Catalytic activation of PS/PMS over Fe-Co bimetallic oxides for phenol oxidation under alkaline conditions [J]. Applied Surface Science, 2021, 562:https://doi.org/10.1016/j.apsusc.2021.150134

[15] Yue L, Hao L, Zhang J, et al. Oxygen-enriched vacancy Co_2MnO_4 spinel catalyst activated peroxymonosulfate for degradation of phenol: Non-radical dominated reaction pathway [J]. Journal of Water Process Engineering, 2023, 53: 1038. https://doi.org/10.1016/j.jwpe.2023.103807

[16] Lu Y, Zhang W, Yang F, et al. Tailored oxygen defect coupling composition engineering $Co_xMn_2O_4$spinel hollow nanofiber enables improved Bisphenol A catalytic degradation [J]. Separation and Purification Technology, 2022, 282: 120 https://doi.org/ 10.1016/j.seppur.2021.120051

[17] Zhao H, Liu Y, Wu D, et al. Multi-pathway on peroxymonosulfate activation by single cobalt atoms incorporated on CuO with enriched oxygen vacancies for high-efficient oxidation of tetracycline [J].Environmental Pollution, 2023, 335: https://doi.org/10.1016/j.envpol.2023.122298

[18] Wang Y, Ji H, Liu W, et al. Novel $CuCo_2O_4$ composite spinel with ameso-macroporous nanosheet structure for sulfate radical formation and benzophenone-4 degradation: interface reaction, degradation pathway, and DFT calculation [J]. ACS Applied Materials & Interfaces, 2020, 12(18):20522-35.https://doi.org/10.1021/acsami.0c03481

[19] Deng J, Xu M, Qiu C, et al. Magnetic $MnFe_2O_4$ activated peroxymonosulfate processes for degradation of bisphenol A: Performance, mechanism and application feasibility [J]. Applied

Surface Science, 2018, 459: 138-4 https://doi.org/10.1016/j.apsusc.2018.07.198

[20] Xu P, Xie S, Liu X, et al. Efficient removal of tetracycline using magnetic $MnFe_2O_4/MoS_2$ nanocomposite activated peroxymonosulfate: Mechanistic insights and performance evaluation [J].Chemical Engineering Journal, 2024, 480: 14. https://doi.org/10.1016/j.cej.2023.148233

[21] Su, Yiping, Yangke Long, Shinyin Zhao, et al. Reduced Fe, Mn-based catalyst with dual reaction sites for rapid decolorization treatment via Fenton-like reactions. Applied Surface Science 616 (April 2023):156522. https://doi.org/10.1016/j.apsusc.2023.156522

[22] Hu F, Liu Y, Shi X, et al. Removal of organic contaminants by starch-derived porous carbon via peroxymonosulfate activation: The role of N doping and Fe/Mn loading [J]. Colloids and Surfaces A: Physicochemical and Engineering Aspects, 2022, 649: 12952. https://doi.org/10.1016/j.colsurfa.2022.129520

[23] Zhao L, Zhang J, Zong Y, et al. Novel insights into Co synergy and electron-transfer pathways during the oxidation of contaminants by Cu-$OOSO_3$- in $CuCo_2O_x$/peroxymonosulfate system [J].Journal of Environmental Chemical Engineering, 2023, 11(2): https://doi.org/10.1016/j.jece.2023.109594

[24] Huang G-X, Wang C-Y, Yang C-W, et al. Degradation of Bisphenol A by peroxymonosulfate catalytically activated with $Mn1.8Fe_{1.2}O_4$ nanospheres: synergism between Mn and Fe [J].Environmental Science & Technology, 2017, 51(21): https://doi.org/10.1021/acs.est.7b03007

[25] Du J, Bao J, Liu Y, et al. Facile preparation of porous Mn/Fe_3O_4 cubes as peroxymonosulfate activating catalyst for effective bisphenol A degradation [J]. Chemical Engineering Journal, 2019,376: https://doi.org/10.1016/j.cej.2018.05.177

[26] Chen Y, Liu Y, Zhang L, et al. Efficient degradation of imipramine by iron oxychloride-activated peroxymonosulfate process [J]. Journal of Hazardous Materials, 2018, 353: 18-25. https://doi.org/10.1016/j.jhazmat.2018.03.050

[27] Xu S, Wen L, Yu C, et.al. Activation of peroxymonosulfate by $MnFe_2O_4$@BC composite for bisphenol A Degradation: The coexisting of free-radical and non-radical pathways[J]. Chemical Engineering Journal, 2022, 442: 136250. https://doi.org/10.1016/j.cej.2022.136250

[28] Y. Zhao, M. Song, Q. Cao, P. Sun, Y. Chen, F. Meng, The superoxide radicals' production via persulfate activated with $CuFe_2O_4$@Biochar composites to promote the redox pairs cycling for efficient degradation of o-nitrochlorobenzene in soil, J Hazard Mater 400 (2020), 122887, https://doi.org/10.1016/j.jhazmat.2020.122887

[29] X. Zhou, L. Kong, Z. Jing, S. Wang, Y. Lai, M. Xie, L. Ma, Z. Feng, J. Zhan, Facile synthesis of superparamagnetic beta-CD-$MnFe_2O_4$ as a peroxymonosulfate activator for efficient removal of 2,4- dichlorophenol: structure, performance, and mechanism, J Hazard Mater 394 (2020), 122528, https://doi.org/10.1016/j.jhazmat.2020.122528

[30] Guo C, Cheng M, Zhang G, et al. Degradation of organic contaminants by peroxymonosulfate activated with zeolitic imidazolate framework-based catalysts: performances, mechanisms and stability [J]. Environmental Science: Nano, 2023, 10(6): 152.https://doi.org/10.1039/d3en00007a

[31] H. Fu, S. Ma, P. Zhao, S. Xu, S. Zhan, Activation of peroxymonosulfate by graphitized hierarchical porous biochar and $MnFe_2O_4$ magnetic nanoarchitecture for organic pollutants degradation: Structure dependence and mechanism, Chem. Eng. J. 360 (2019) 157–170, https://doi.org/10.1016/j.cej.2018.11.207

[32] Y. Yao, Y. Cai, F. Lu, F. Wei, X. Wang, S. Wang, Magnetic recoverable $MnFe_2O_4$ and $MnFe_2O_4$-graphene hybrid as heterogeneous catalysts of peroxymonosulfate activation for efficient degradation of aqueous organic pollutants, J Hazard Mater 270 (2014) 61–70, https://doi.org/10.1016/j.jhazmat.2014.01.027

[33] Wang X, Zhang C, Ma Y, et al. Readily separable and stable $CoFe_2O_4$ beads for activating peroxymonosulfate to degrade lomefloxacin hydrochloride: Optimization, performance and degradation mechanism [J]. Separation and Purification Technology, 2023, 327: 1249 https://doi.org/10.1016/j.seppur.2023.124975

[34] F. Chen, X.-L. Wu, L. Yang, C. Chen, H. Lin, J. Chen, Efficient degradation and mineralization of antibiotics via heterogeneous activation of peroxymonosulfate by using graphene supported single-atom Cu catalyst, Chem. Eng. J. 394 (2020),124904, https://doi.org/10.1016/j.cej.2020.124904

[35] Ge T, Han J, Qi Y, et al. The toxic effects of chlorophenols and associated mechanisms in fish [J].Aquatic Toxicology, 2017, 184: 78-93. https://doi.org/10.1016/j.aquatox.2017.01.005

[36] Liang W, Shen C, Zhu Y, et al. Enhanced activation of PMS by a novel $MnFe_2O_4$@N-PC-GM composite for rapid 1-naphthol degradation: Formation and mechanism of singlet oxygen [J].Journal of Environmental Chemical Engineering, 2023, 11(6). https://doi.org/10.1016/j.jece.2023.111579

[37] X. Duan, H. Sun, Z. Shao, S. Wang, Nonradical reactions in environmental remediation processes: Uncertainty and challenges, Appl. Catala. B 224 (2018)973–982, https://doi.org/10.1016/j.apcatb.2017.11.051

[38] Sahoo B, Sahu S K, Nayak S, et al. Fabrication of magnetic mesoporous manganese ferrite nanocomposites as efficient catalyst for degradation of dye pollutants [J]. Catalysis Science &Technology, 2012, 2(7). https://doi.org/10.1039/c2cy20026k

[39] Descorme C. Catalytic wastewater treatment: Oxidation and reduction processes. Recent studies on chlorophenols [J]. Catalysis Today, 2017, 297: 324-34. https://doi.org/10.1016/j.cattod.2017.03.039

[40] Z. Dong, Q. Zhang, B.-Y. Chen, J. Hong, Oxidation of bisphenol A by persulfate via Fe_3O_4-α-MnO_2 nanoflower-like catalyst: Mechanism and efficiency, Chem. Eng. J.357 (2019) 337–347, https://doi.org/10.1016/j.cej.2018.09.179

[41] X. Zhang, M. Feng, R. Qu, H. Liu, L. Wang, Z. Wang, Catalytic degradation of diethyl phthalate in aqueous solution by persulfate activated with nano-scaled magnetic $CuFe_2O_4$ /MWCNTs, Chem. Eng. J. 301 (2016) 1–11, https://doi.org/10.1016/j.cej.2016.04.096

[42] C. Cai, H. Zhang, X. Zhong, L. Hou, Ultrasound enhanced heterogeneous activation of peroxymonosulfate by a bimetallic Fe-Co/SBA-15 catalyst for the degradation of Orange II in water, J Hazard Mater 283 (2015) 70–79, https://doi.org/10.1016/j.jhazmat.2014.08.053

[43] L. Deng, Z. Shi, Z. Zou, S. Zhou, Magnetic EDTA functionalized $CoFe_2O_4$ nanoparticles (EDTA-$CoFe_2O_4$) as a novel catalyst for peroxymonosulfate activation and degradation of Orange G, Environ Sci Pollute Res Int 24 (2017)11536–11548, https://doi.org/10.1007/s11356-017-8811-1

[44] H. Zhang, X. Liu, C. Lin, X. Li, Z. Zhou, G. Fan, J. Ma, Peroxymonosulfate activation by hydroxylamine-drinking water treatment residuals for the degradation of atrazine, Chemosphere 224 (2019) 689–697, https://doi.org/10.1016/j.chemosphere.2019.02.186

[45] X. Long, S. Yang, X. Qiu, D. Ding, C. Feng, R. Chen, X. JihuaTan, N. Wang, Q.L. Chen,

Heterogeneous activation of peroxymonosulfate for bisphenol A degradation using $CoFe_2O_4$ derived by hybrid cobalt-ion hexacyanoferrate nanoparticles, Chemical Engineering Journal 404 (2021), 127052, https://doi.org/10.1016/j.cej.2020.127052.

[46] Z,.G Zhou,, H.-M. Du, Z. Dai, Y. Mu, L.-L. Tong, Q.-J. Xing, S.-S. Liu, Z. Ao, J.-P. Zou, Degradation of organic pollutants by peroxymonosulfate activated by MnO_2 with different crystalline structures: Catalytic performances and mechanisms, Chem. Eng. J. 374 (2019) 170–180, https://doi.org/10.1016/j.cej.2019.05.170

[47] X. Dong, B. Ren, Z. Sun, C. Li, X. Zhang, M. Kong, S. Zheng, D.D. Dionysiou, Monodispersed $CuFe_2O_4$ nanoparticles anchored on natural kaolinite as highly efficient peroxymonosulfate catalyst for bisphenol A degradation, Appl. Catala. B 253 (2019) 206–217, https://doi.org/10.1016/j.apcatb.2019.04.052

[48] D. Ouyang, Y. Chen, J. Yan, L. Qian, L. Han, M. Chen, Activation mechanism of peroxymonosulfate by biochar for catalytic degradation of 1,4-dioxane: Important role of biochar defect structures, Chem. Eng. J. 370 (2019) 614–624, https://doi.org/10.1016/j.cej.2019.03.235

[49] Y. Ding, X. Wang, L. Fu, X. Peng, C. Pan, Q. Mao, C. Wang, J. Yan, Nonradicals induced degradation of organic pollutants by peroxydisulfate (PDS) and peroxymonosulfate (PMS): Recent advances and perspective, Sci Total Environ 765(2021), 142794, https://doi.org/10.1016/j.scitotenv.2020.142794

[50] Y. Zhang, W. Chu, Cooperation of multi-walled carbon nanotubes and cobalt doped TiO_2 to activate peroxymonosulfate for antipyrine photocatalytic degradation, Sep. Purify. Technol. 282 (2022), 119996, https://doi.org/10.1016/j.seppur.2021.119996

[51] J. You, C. Zhang, Z. Wu, Z. Ao, W. Sun, Z. Xiong, S. Su, G. Yao, B. Lai, N-doped graphite encapsulated metal nanoparticles catalyst for removal of Bisphenol A via activation of peroxymonosulfate: A singlet oxygen-dominated oxidation process, Chem. Eng. J. 415 (2021), 128890, https://doi.org/10.1016/j.cej.2021.128890

[52] Y. Li, S. Ma, S. Xu, H. Fu, Z. Li, K. Li, K. Sheng, J. Du, X. Lu, X. Li, S. Liu, Novel magnetic biochar as an activator for peroxymonosulfate to degrade bisphenol A: Emphasizing the synergistic effect between graphitized structure and $CoFe_2O_4$,Chem. Eng. J. 387 (2020), 124094, https://doi.org/10.1016/j.cej.2020.124094

[53] Xue Yang, Zhi Guo, Xing Chen, Shanshan Xi, Kangping Cui, ed al, Efficient degradation of thiamethoxam pesticide in water by iron and manganese oxide composite biochar activated persulfate [J]. Chemical Engineering Journal.473 (2023),145051. https://doi.org/10.1016/j.cej.2023.145051

[54] Shihu Cao, Yaqi Yin, Shugang Zheng, Chunjin Song, Xinrui Gan ed al, Peroxymonosulfate activation by Ni–Co nanoparticles encapsulated in nitrogen-doped carbon derived from Co-doped Ni metal–organic frameworks for efficient enrofloxacin degradation J Chemical engineering journal.503 (2025).158281. https://doi.org/10.1016/j.cej.2024.158281

[55] Jiankun Zhang, Lei Chen, Xueyang Zhang, Removal of P-nitrophenol by nano zero valent iron-cobalt and activated persulfate supported onto activated carbon,Chem.Eng.J.14 (2022),1387 https://doi.org/10.3390/w14091387

[56] N. Ueda Yamaguchi, R. Bergamasco, S. Hamoudi, Magnetic $MnFe_2O_4$-graphene hybrid composite for efficient removal of glyphosate from water, Chemical Engineering Journal 295 (2016) 391–402, https://doi.org/10.1016/j.cej.2016.03.05

[57] Deng J, Feng S, Ma X, et al. Heterogeneous degradation of Orange II with peroxymonosulfate activated by ordered mesoporous $MnFe_2O_4$ [J]. Separation and Purification Technology, 2016, 167:181-9 https://doi.org/10.1016/j.seppur.2016.04035

Supplementary Files

This is a list of supplementary files associated with this preprint. Click to download.

- Supplementarymaterial.docx